Available online at www.sciencedirect.com
SCIENCE DIRECT®
Biochimica et Biophysica Acta 1663 (2004) 178–187
BIOCHIMICA ET BIOPHYSICA ACTA
BBA
www.bba-direct.com

Electron holography of non-stained bacterial surface layer proteins

P. Simon[a,*], H. Lichte[a], R. Wahl[b], M. Mertig[b], W. Pompe[b]

[a] *Triebenberg Laboratory, Institute of Structure Physics, Dresden University, D-01062 Dresden, Germany*
[b] *Max Bergmann Center of Biomaterials and Institute of Materials Science, Dresden University, D-01069 Dresden, Germany*

Received 8 August 2003; received in revised form 9 March 2004; accepted 16 March 2004

Abstract

We report transmission electron microscopy (TEM) investigations on bacterial surface layers (S-layers) which belong to the simplest biomembranes existing in nature. S-layers are regular 2D protein crystals composed of single protein or glycoprotein species. In their native form, S-layers are weak phase objects giving only poor contrast in conventional TEM. Therefore, they are usually examined negatively stained. However, staining with heavy metal compounds may cause the formation of structural artefacts. In this work, electron microscopy studies of non-stained S-layers of *Bacillus sphaericus* NCTC 9602 were performed. Compared to other proteins, these S-layers are found relatively stable against radiation damage. Electron holography was applied where information about phase and amplitude of the diffracted electron wave is simultaneously obtained. In spite of small phase shifts observed, the phase image reconstructed from the hologram of the non-stained S-layer is found to be sensitive to rather slight structure and thickness variations. The lateral resolution, obtained so far, is less than that of conventional electron microscopy of negatively stained S-layers. It corresponds to the main lattice planes of 12.4 nm observed in the reconstructed electron phase image. In addition, as a unique feature of electron holography the phase image provides thickness information. Thus, the existence of double layers of the protein crystals could be easily visualized by the height profile of the specimen.

Keywords: Protein membrane; S-layer protein; Transmission electron microscopy; Electron holography

1. Introduction

Regular bacterial surface proteins (S-layer) are quasi two-dimensional crystals with different lattice symmetries of periodically arranged proteins or glycoproteins, which form the outermost part of the cell envelope of various bacteria and archeae [1]. On average, S-layers are 5–15 nm thick. It can be isolated from the bacteria by means of biochemical methods. The isolated protein is able to re-crystallize into two-dimensional lattices with different morphologies depending on the environmental conditions. Thus, there appear mono- and multi-layers as well as cylindrically shaped structures at the micrometer scale.

There is a lively interest in the determination of the biological functions of the S-layer, which is not yet fully understood [2,3]. Because of the high energy involved to produce the S-layer protein within the living cell, the function must be essential. The strong resistance of several of these simple biological membranes to extreme environmental conditions, such as high temperatures up to 140 °C, pH down to 0.5 or high ionic strength, seems to indicate that S-layers act as a protective shield of the living cell [2]. An additional evidence for this assumption is the higher resistance of *B. cereus* cells with S-layer against Gamma-radiation than *B. cereus* strains without S-layer reported by Kotiranta et al. [4].

The stability, isoporosity and highly regular lattice structure with the small lattice constants of 2.5–35 nm predestinate S-layers for the application in the field of biomolecular nanotechnology. In the past years it has been shown that they can be used for example as biomolecular templates for the formation of inorganic nanostructures like metallic cluster arrays [5–13]. To gain new structural insights and information of the characteristics of the biological samples, which will be

---

* Corresponding author. Present address: Max Planck Institute for Chemical Physics of Solids, Nöthnitzer Str. 40, 01187 Dresden, Germany. Tel.: +49-351-4646-4209; fax: +49-351-4646-3002.
E-mail address: simon@cpfs.mpg.de (P. Simon).

0005-2736/$ - see front matter © 2004 Elsevier B.V. All rights reserved.
doi:10.1016/j.bbamem.2004.03.005

useful for future applications, we aim at imaging such S-layer systems by means of electron holography in their non-stained state, i.e. without the application of conventional heavy metal contrast agents.

In this work, we focussed on the S-layer protein isolated from *Bacillus sphaericus* NCTC9602 which was used as a biotemplate for palladium or platinum nanoparticles [12,13]. For a better understanding of the underlying mechanisms of cluster formation, it is essential to correlate the positions of growing clusters with the protein structure. This problem can be solved by conventional transmission electron microscopy (TEM) only by indirect methods. Up to now, it is not possible to make visible the protein structure and the cluster simultaneously in the transmission electron microscope. The reason is that biological samples are mainly composed of elements such as carbon, hydrogen, oxygen and nitrogen with low atomic numbers. In the case of these light elements, only a slight phase shift of the electron wave in the range of $2\pi/100$ up to $2\pi/20$ [14–16] contributes to contrast formation. As consequence, the induced phase shift φ, given by the product of sample thickness and mean inner potential, will also be rather small and therefore provides poor contrast.

Contrast enhancement by negative staining, which means the embedding of the sample in heavy metal compounds [17–19], or specific defocus [20–22] are the most popular microscopic methods to visualize weak phase structures. Negative staining can cause artefacts by selective binding and can therefore result in different structure information for different staining compounds [23]. Furthermore, the grain size of about 10–15 Å of the heavy metal compounds determines the lower limit to the imaging of finer object details [24].

In conventional electron microscopy, the image intensity $I(x) = b(x)b^*(x) = A^2(x)$ is recorded, whereas the image phase $\Phi(x)$ is lost. Therefore, by means of a suitable defocus, the object phase $\varphi(x)$ has to be directed into the image amplitude $A(x)$ to be recordable at a sufficient contrast. However, if strong defocus is applied, only a fraction of the spacings of interest is transferred with a sufficient contrast, whereas due to the oscillations of the phase contrast-transfer function (PCTF), a remarkable loss of resolution is found; furthermore artefacts like delocalization show up. Additionally, at strong underfocus, the appearance of Fresnel fringes at the edges of the sample makes the image interpretation quite difficult.

These methods of contrast enhancement are not suitable for biotemplating systems consisting of organic and inorganic matter. That's why the indirect method mentioned above has to be used consisting of two steps: firstly, one has to examine the protein in order to obtain the crystal structure and also gain detailed information of the monomeric units. Then, the structure of the non-stained S-layer covered by the regular array of the inorganic particles has to be compared with the stained micrograph in order to locate the binding site [11].

These difficulties can be avoided, if one is able to record the phase of the sample by electron holography in the transmission electron microscope [25–28]. By superimposing a reference wave with the object wave, electron holography becomes sensitive to rather slight structure and thickness variations. The phase image contains all important structure information and one obtains good contrast even for small phase shifts without staining. In this way, one could observe the protein crystal and the cluster array of inorganic nanoparticles simultaneously. In this paper, the first step is taken and off-axis electron holography is performed on non-stained protein samples.

In spite of the mentioned advantages, there are only a few publications dealing with electron off-axis-holography of biological samples. Firstly, Kawasaki et al. [29] reported holographic investigations of unstained ferritin molecules. Other biological specimens observed by this technique were the tobacco mosaic virus (TMV) [30,31], bacterial flagellum filaments [32], virus-like particles of human immunodeficiency virus (HIV) [33], Semliki Forest virus [33], T5 Phage [33] and bacterial hexagonally packed intermediate (HPI) layer [33].

In all these works, the shape of the specimen could be imaged but not the inner structure or finer structural details within the biomolecules, with the exception of the HPI, where the periodicity of the crystal layer could be imaged with a lattice constant of about 18 nm. Therefore, the resolution of the method can be estimated by the dimensions of the investigated molecules. The sizes varied about, e.g. 9 nm for ferritin, 18 nm for TMV, 24 nm for the bacterial flagellum filaments and 65 nm (head) or 20 nm (tail) for the T5 Phage.

An additional advantage of electron holography is given by its sensitivity to thickness and materials variations. As a consequence, we can measure the regularity of the topography of such non-stained crystal sheets. A further investigation of the template samples would provide information about the thickness changes induced by the deposited nanoparticles.

One should mention that there exists another electron holographic method, the so-called in-line or point projection holography. This technique does not need a biprism and works at low electron energies and as a consequence, the knock-on beam damage for biological molecules should be minimized. Some work on biological systems were performed such as DNA [34,35] and TMV [36], and the method is still in progress.

When one performs electron microscopy on organic and biological materials, beam damage will play a decisive role [37–42]. Therefore, the attainable resolution is not given by the point resolution of the microscope but by the critical dose of the sample. Various undesirable phenomena will occur such as loss of long range order accompanied by chemical decomposition, mass loss, and decrease of mechanical stability. Finally, with the higher brightness of the field emission guns (FEG) and higher acceleration voltage, the probability of knock-on damages will also increase for organic or biological samples. Therefore, it is important to estimate roughly the influence of the electron beam damage on the non-stained S-layer.

2. Materials and methods

2.1. Preparation of S-layer films

The S-layer protein was isolated from *B. sphaericus* NCTC 9602 cells. The cell cultivation conditions, protein purification and re-crystallization in solution are described elsewhere [12]. The concentration of the crystallized S-layer suspension amounted to about 10 mg per ml.

For electron microscopy, 50 μl of the suspension was diluted in 1 ml H_2O bidest, and a drop of this was placed onto the electron microscopy grid. After 1 min, the excess was removed by a blotting paper and thereafter dried on air. The electron microscopy grids (Quantifoil, Jena, Germany) were covered with a holey carbon film with hole diameters ranging from 4 up to 8 μm separated by thin bars. Free-standing films of S-layer protein crystals stretch across the holes. Larger holes are more favourable because often they are not completely covered with S-layer, leaving adjacent vacuum area for the reference wave.

After the drying process, the S-layers were covered on one side by an evaporated carbon layer with a thickness of about 2 nm in order to avoid charging.

2.2. Electron microscopy

Conventional TEM was performed with a Philips CM200 FEG/ST Lorentz electron microscope at an acceleration voltage of 200 kV. In order to gain a larger field of view of about 300 × 300 nm^2, the regular objective lens has to be switched off and the Lorentz lens has to be activated instead. The so-called Lorentz or Twin 2 lens is a mini lens, embedded in the lower pole piece of the objective lens. It was designed for imaging of magnetic and biological objects with increased contrast. The focal distance of the Twin 2 lens is 12 × and the spherical aberration 6000 × larger than of the conventional objective; therefore, the theoretical point resolution amounts to about 2.2 nm.

2.3. Stability measurements

Stability measurements were performed at different electron doses. The conventional image was recorded at strong defocus in order to obtain sufficient contrast. By increasing the accumulated electron dose, successively intense beam damage was observed. The induced damage was evaluated by the fading of the diffraction spots, which were determined by Fast Fourier Transform (FFT) of the direct image. The window size for evaluation of the intensities of the diffraction spots amounted to $(0.0239 \times 0.0239)\ \mathrm{nm}^{-2}$ and the number of electrons per area was read out for each reflection. However, these evaluations of the diffraction spot fading were not background corrected.

2.4. Electron holography

The off-axis electron holography was performed on the electron microscope Philips CM200 FEG/ST Lorentz with an experimental set-up described elsewhere [16]. The holograms were recorded in-focus with a biprism voltage of about 130 V. At the magnification of 30,000 × an interference fringe width of 4 nm was obtained corresponding to a possible resolution of 8 nm in the reconstructed electron phase image. The holograms were evaluated by the software Digital Micrograph 3.3.1 (Gatan).

3. Results

3.1. Stability measurements

In general, proteins are extremely beam-sensitive and are already destroyed by a dose of about 1 e $\mathrm{\AA}^{-2}$ [37]. In order to determine the critical dose, we observed the decay of lattice order by direct imaging of the non-stained layer specimen at strong defocus at different applied dose. When applying a dose rate of 77 e $\mathrm{\AA}^{-2}\ \mathrm{s}^{-1}$ the crystalline order is weakened remarkably after 1 min and will be strongly damaged after 2–3 min (Fig. 1). In order to estimate roughly the beam damage quantitatively, the intensities of the diffraction spots in the FFT has to be compared with increasing accumulated dose (inset, Fig. 1). The first read-out value of the applied dose was set to be zero. However, one has to keep in mind that the sample was pre-irradiated in order to find and to focus the region of interest.

One would expect that the substructure corresponding to smaller spacings may already be damaged at the very beginning during the beam exposure, whereas the biggest lattice spacings of the (10) and (01) planes should be still preserved. A survey of fading of all reflections by increased dose is given in Table 1.

As the results of Table 1 show, there is no clear finding that finer structure details are destroyed first. For example, the large spacing of 12.5 nm corresponding to (10) almost reaches the critical dose with 42% of the initial intensity at an accumulated dose of 13,860 e $\mathrm{\AA}^{-2}$ (I_3), whereas the (02) reflection at 6.2 nm still shows a value of 80% of the initial intensity I_0. Reflections (10) and (01) should have the same intensity, and the same holds for (20), (02), (21) and (12) diffraction spots. Presumably due to mistilt, they show different intensities thus averaging of the intensities was not considered. Another astonishing finding is that, after an irradiation dose of about 4700 e $\mathrm{\AA}^{-2}$ (I_1), the intensity of the first-order diffraction spots (10) and (01) even increases

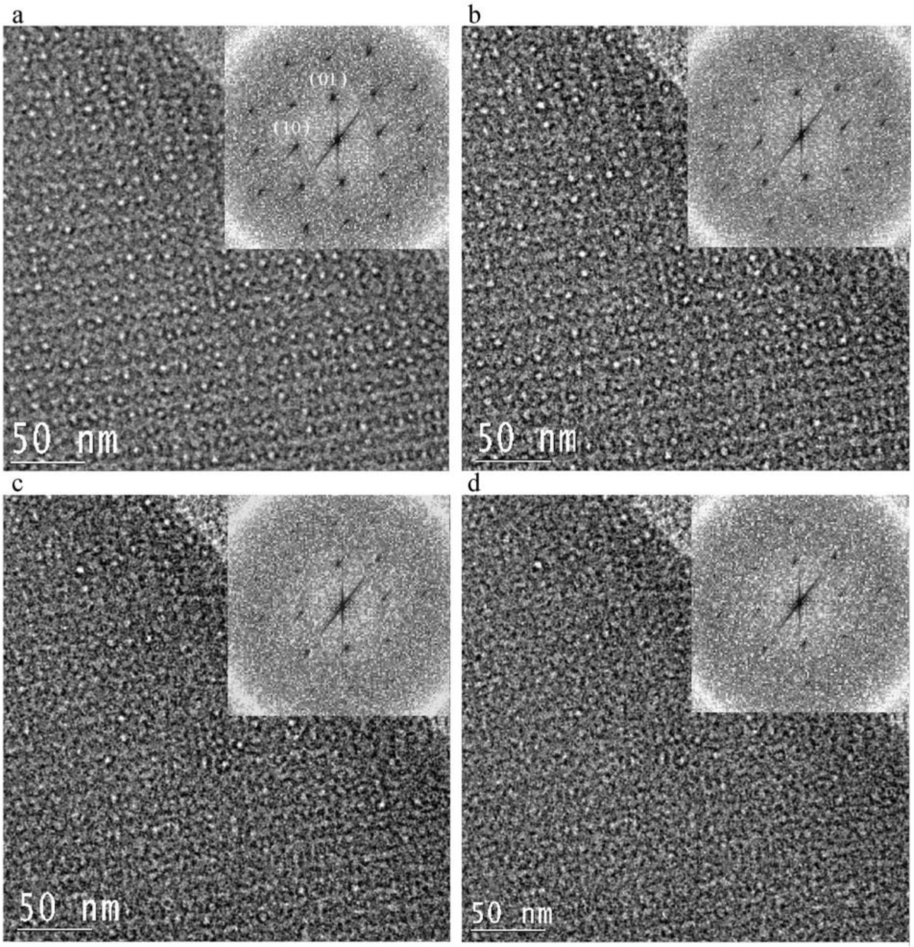

Fig. 1. Beam damage of non-stained S-layer protein exposed to a dose rate of 77 e Å^{-2} s^{-1}. At certain time intervals micrographs were taken of the same sample area at strong defocus. The accumulated dose increased in the following sequence: (a) $t = 2$ s, D ~ 0 e Å^{-2}. (b) $t = 60$ s, D ~ 4800 e Å^{-2}. (c) $t = 120$ s, D ~ 9600 e Å^{-2}. (d) $t = 180$ s, D ~ 14,400 e Å^{-2}. The insets display the processed FFT. Obviously, the diffraction spots are fading away by increasing the accumulated dose. After 3 min the critical dose for the (01) spot is almost reached.

compared to zero dose at 0 e Å^{-2} as demonstrated by the plot in Fig. 2. Similar behaviour was found by Ohno [43] for behenic acid by electron diffraction, whereas Knapek at al. [44] detected even a statistic behaviour for L-valine at low temperatures. The rise of initial intensity during irradiation was explained by crystal tilt caused by charging effects and local heating. However, in our experiment, this effect lies within 15% deviation.

Table 1
Number of electrons in different reflections in dependence of the dose cumulated in the S-layer crystal

(hk)	I_0 Dose 0 (e Å^{-2})	I_1 Dose 4690 (e Å^{-2})	I_2 Dose 9240 (e Å^{-2})	I_3 Dose 13,860 (e Å^{-2})	I_3/I_0 (%)
(10)	6.435.000	7.408.000	5.159.000	4.814.000	75
(20)	4.802.000	2.874.000	2.728.000	1.214.000	25
(01)	5.762.000	5.949.000	4.441.000	2.422.000	42
(02)	6.706.000	2.706.000	3.113.000	5.368.000	80
(11)	10.832.000	6.331.000	5.421.000	4.509.000	42
(21)	6.118.000	5.057.000	6.678.000	4.023.000	66
(12)	6.046.000	4.052.000	2.586.000	3.465.000	57

The window size for evaluation of the intensities of the diffraction spots amounts to (0.0239 × 0.0239) nm^{-2}.

By direct imaging, one is able to obtain a coarse assessment of the critical dose for the S-layer protein crystal at room temperature. The estimation shows that it should be possible to perform electron holography on this S-layer system and to image the unit cells of 12.5×12.5 nm^2. Former measurements by electron diffraction on glucose-embedded bacteriorhodopsin [42] show that the finer structural detail of 7 Å vanishes at a dose of 1.4 e Å^{-2}, and that the 3 Å reflection already reaches the critical dose below 1 e Å^{-2} at room temperature. In a very early paper by Glaeser and Taylor [45] the beam damage of glucose-embedded catalase crystals is described. As they found out, the logarithm of critical dose is linear with the achievable resolution. However, in their diagram for room temperature, the biggest spacing corresponds to only 2.5 nm. If one extrapolates their findings to 12.5 nm, which complies to the biggest spacing for the S-layer, we find a critical dose of about only 6 e Å^{-2}. In the beam damage experiments, where the much higher dose

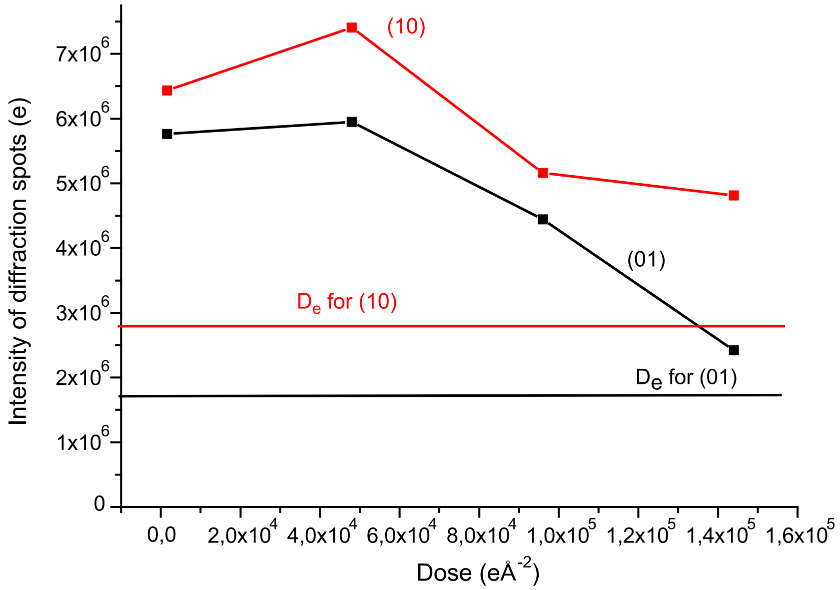

Fig. 2. Beam damage of the non-stained S-layer protein exposed to a dose rate of 77 e Å^{-2} s^{-1}. The intensities of the diffraction spots of Fig. 1a–d are plotted versus the applied dose for the (10) and (01) lattice planes. The lines mark the levels of critical doses D_e of the corresponding lattice planes.

rate of 77 e Å^{-2} s^{-1} was applied, we had some different circumstances. For example, in our experiments we did not apply embedding but we used the as-dried samples and, additionally, we evaporated a protective thin carbon layer onto the sample. Further on, we worked at a higher accelerating voltage and we could make use of single electron detection by our CCD camera. Weierstall and Lichte [31] applied an accumulated dose from 15 up to 45 e Å^{-2} in order to check the beam resistance of vitrified TMV at 4 Kelvin. Whereas at 15 e Å^{-2} the finer structure could be preserved structure destruction and bubble formation occurred at a dose of 45 e Å^{-2}.

The reason for the drastically enhanced dose rate of 77 e Å^{-2} s^{-1} for the beam damage experiment was that we wanted to reach the region of the critical dose of the S-layer. On the other hand, for the holography experiments, we reduced the dose rate to about 4 e Å^{-2} s^{-1} in order protect the sample. From our beam damage experiment, it can be concluded that S-layers are notably stable against beam damage.

3.2. Estimations of the phase shifts produced by biological samples

As criterion whether it is possible to image the biological sample under investigation, we have to estimate the phase shift produced by the specimen. The phase shift is proportional to the product of the mean inner potential U_i of the sample and its thickness d along the incident beam

$$\Delta\phi = C_E U_i d \tag{1}$$

C_E = interaction parameter [V^{-1} nm^{-1}].

For a high tension of 200 kV, the parameter C_E amounts to 0.0073 V^{-1} nm^{-1} at a wavelength of $\lambda = 2.5$ pm. In this way, we are able to assess beforehand, whether there is a sufficient phase shift needed for the signal detection.

The following calculations for the expected phase shift are performed under the assumption that the S-layer of *B. sphaericus* NCTC 9602 investigated in this study features a thickness of 5 nm as determined by scanning force microscopy [46]. Assuming the inner potential of the S-layer to be equal to that of polystyrene of $U = 8.2$ V [47] a resulting phase shift of $\Delta\phi = 0.33$ rad by a single S-layer is obtained. For the mean inner potential of the S-layer, the value of polystyrene was taken, since there are no experimental values of inner potentials of biological samples available. Till today, there exist only one organic compound, which experimental inner potential is known and this is polystyrene. The value of $\Delta\phi \sim 0.33$ rad lies about four and a half times above the critical phase shift of ~ 0.07 rad, which could just be detected in the microscope [15]. Therefore, one can expect that such kind of objects could also be observed adequately well in the holographic electron phase image.

3.3. Electron holography

In Fig. 3a, the reconstructed electron phase image of the crystalline S-layer is shown. The calculated diffraction pattern (power spectrum) features four spots corresponding to a square lattice with a spacing of 11 nm, which is to some extent smaller than measured by the negative staining method of 12.5 nm. This shrinkage of 12% could be caused by deformation of the S-layer lattice during the drying process, if we take into account mechanical stress, since the S-layer sheet spans over vacuum and hence is not supported by the carbon substrate. Finally we have to consider stress due to irradiation. Deformation and shrinkage of protein crystal sheets were also found on stained and

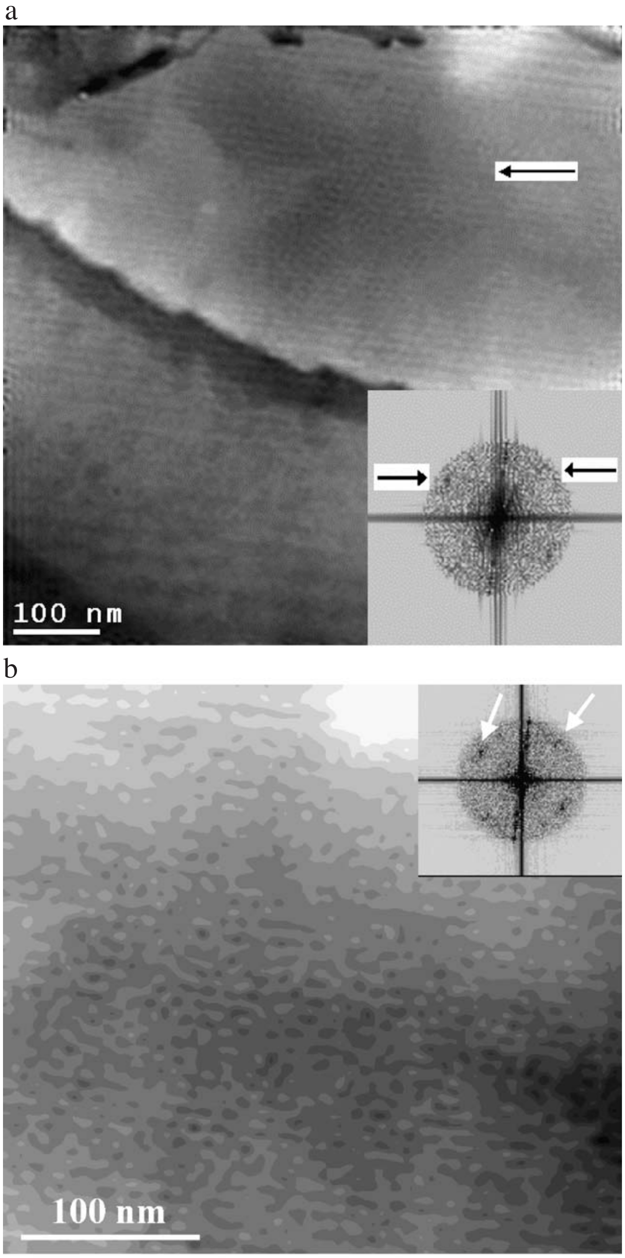

Fig. 3. (a) Reconstructed phase image of the unstained crystal lattice of the surface layer protein. The position of the crystal sheet is indicated by the black arrow. At the bottom up to the centre, the carbon support film appears confined by a dark edge, whereas the protein film above spans over vacuum. The calculated diffraction pattern (power spectrum) features four reflections (black arrows) corresponding to the main lattice spacings of 11 nm. Furthermore, the crystal lattice show the typical angle of 45° with respect to the boundary of the protein sheet. This finding is well known from stained samples. (b) Zoomed phase image of the crystalline region marked with the arrow in panel a. The inset at the right top indicates the corresponding FFT.

free-standing catalase crystal layers and on a freeze-dried and free-standing protein HPI-layer [33]. The dose rate for recording the hologram amounted to 3.6 e $Å^{-2}$ s^{-1} which is about 21 times smaller compared to the dose rate applied in the beam damage experiment. The magnification is 35,500 × and the contrast of the hologram fringes gave 11%. Fig. 3b is showing a zoomed area of the protein crystal sheet marked with a black arrow in Fig. 3a. The inset is showing the Fast Fourier Transform (FFT) with the (10) and (01) reflection corresponding to 1/11 nm^{-1}.

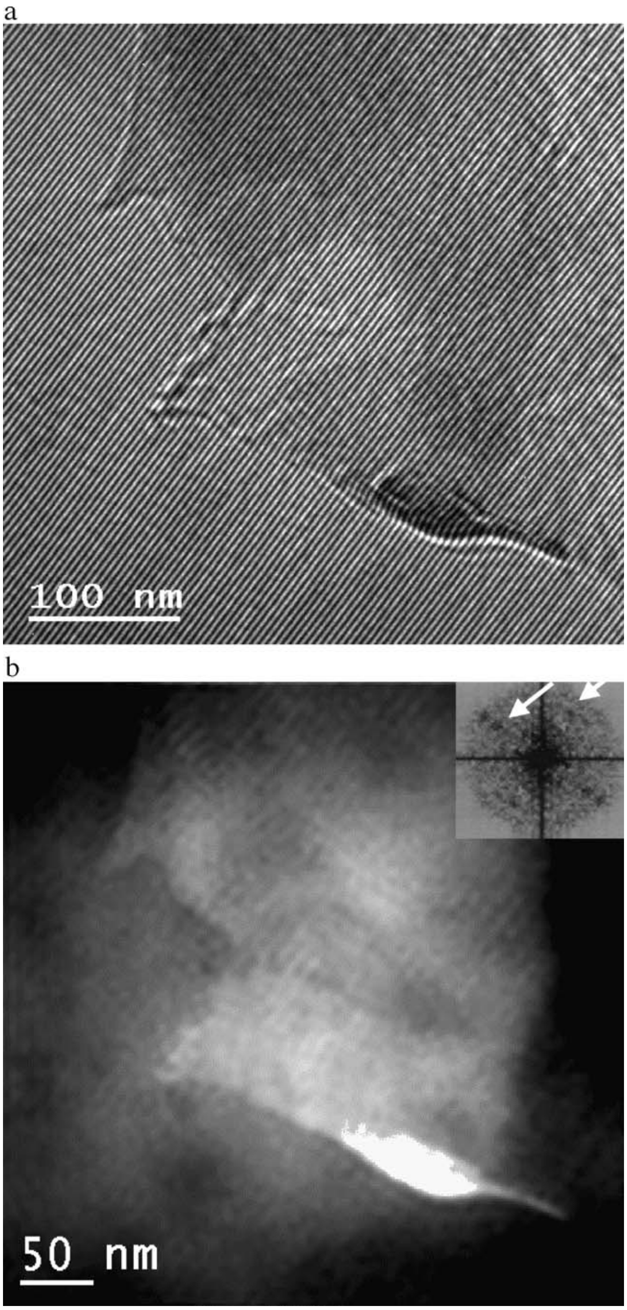

Fig. 4. (a) Electron hologram of the unstained crystal sheet of surface layer protein at a magnification of 61,000 × recorded with a dose rate of 4 e $Å^{-2}$ s^{-1}. The resolution is given by the double of the interference fringe periodicity of 4 nm. The contrast of the fringes amounts to 20%. (b) Reconstructed phase image of the unstained crystal lattice of surface layer protein as shown in panel a. The inset at the right top is showing the power spectrum of the crystal with 'diffraction spots' corresponding to 1/11.3 $(nm)^{-1}$.

A typical electron hologram of the S-layer is shown in Fig. 4a. The resolution is determined by the double-spacing of the interference fringe periodicity and amounts to 8 nm. It is important to adjust high contrast of the interference pattern in order to gain sufficient phase sensitivity in the corresponding reconstructed phase image (Fig. 4b). In this way, we obtain a phase micrograph at just focus imaging of the edges of the crystal sheet without blurring. The topography is nicely reproduced in the phase image showing a strong waviness of the crystal sheet as indicated by the bright areas corresponding to thicker sample regions and darker regions which represent the thinner parts.

By means of electron holography on stained samples the double layer structure of the adsorbed S-layer sheets could be already proved. Electron holography is sensitive to the thickness of the sample (see Eq. (1)), thus the stepwise change from the monolayer to the double layer could be measured by the height profile [13]. One layer produces a phase shift of about 0.5 rad for these stained samples.

Under specific conditions the S-layer proteins crystallize into cylindrically shaped assemblies of several hundred nanometers in diameter and a few micrometers in length [12]. If a suspension, containing such cylinders, is adsorbed onto a holey carbon grid, one can observe that some of them were spanned as flat double layers over the holes. Because the ends of the cylinders are frayed, these positions are suitable for detecting the transition from mono- to double layered areas.

In this work, we succeeded in imaging these steps on non-stained samples by electron holography (Fig. 5a). In Fig. 5b(1) the phase profile of a double layer step is shown taken from the region labeled 1 in Fig. 5a. The phase difference between the vacuum level and the double layer amounts to 0.6 rad, which is in good agreement with the value estimated in Section 3. At the region marked by label 2 in Fig. 5a, the origin of a disruption of the crystal sheet is shown. The two fibres which are spanned between the two ripped parts display a phase shift of 0.3 rad respectively. This value corresponds to a single layer shift as estimated in Section 3. In order to assess the thickness variations along the long axis of the protein sheet, a phase profile was drawn at the area marked with the number 3 in Fig. 5a. As can be read from the phase profile, some

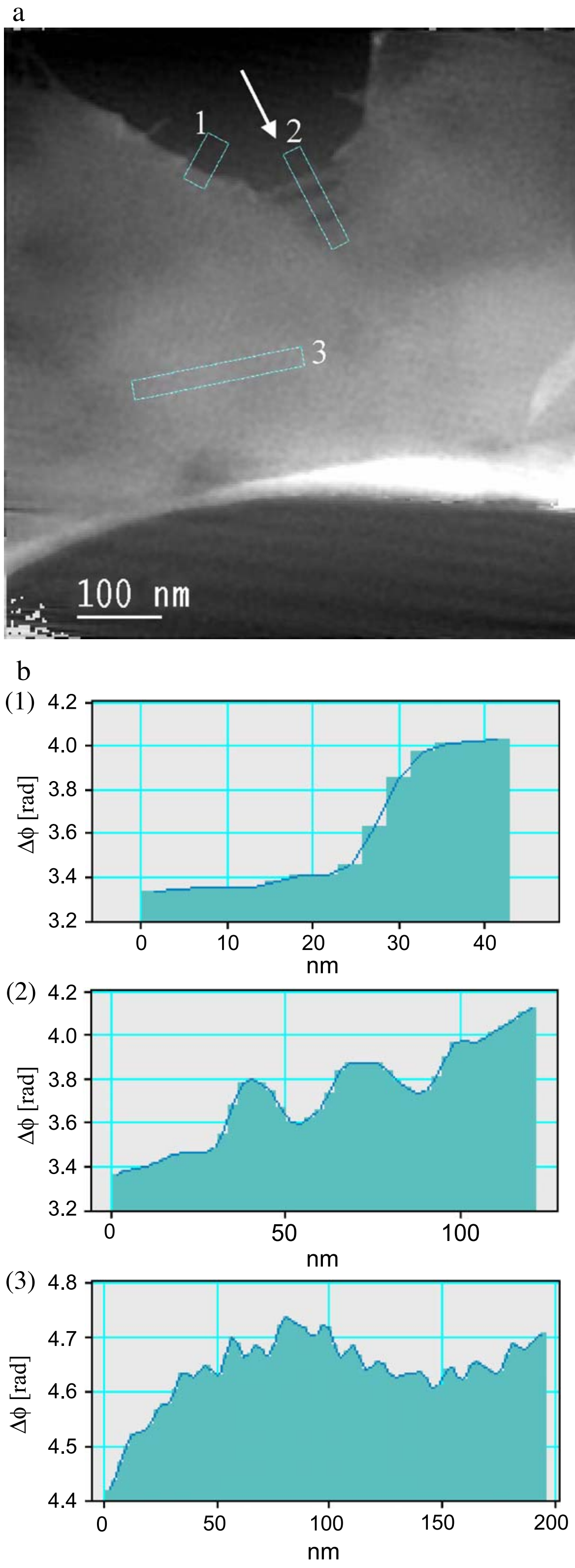

Fig. 5. (a) Reconstructed phase image of electron hologram of the surface layer protein crystal sheet. The bright area represents the S-layer, whereas the dark areas at the top and the bottom represent vacuum. The protein self-assembly product displays a disruption in the middle at the top marked by the white arrow. The double layer constitution of the crystal sheet is demonstrated by the height profile 1 (panel b(1)), which runs normal to the edge of the sheet. For area 2, a phase profile in panel b(2) is drawn in order to measure the thickness of the 'fibrils' spanning over the disruption edges. The phase profile of area 3 is displaying the roughness variation along the sheet main direction. (b1) Phase profile of region 1 of panel a normal to the edge of the sample. The difference between the vacuum level at the left of 3.4 rad and the double layer with 4.0 rad on the right amounts to 0.6 rad. This finding shows a good agreement with the estimated value of ∼ 0.66 rad given in Section 3. (b2) Phase profile of region 2 of panel a at the disruption origin. The two 'fibres", which are spanned between the two ripped parts show a phase shift of 0.3 rad corresponding to a monolayer thickness. Vacuum is situated on the left at ∼ 3.4 rad level. (b3) Phase profile of region 3 of panel a drawn parallel to the sheet main direction. The maximum deviation amounts to 0.3 rad corresponding to a thickness variation of ∼ 5 nm along 200 nm.

areas are very smooth, i.e. the maximum roughness amounts to 5 nm across 200 nm width parallel to the sheet long axis.

In order to get an assessment about the noise limit of the phase, one has to look at an area, which displays frayed crystal sheets (Fig. 6a). The height profile (Fig. 6b) was taken from the region of interest marked in Fig. 6a. Two steps can be clearly recognised. Assuming a mean inner potential of 8.2 V, each step represents the thickness of a double layer. Fourfold thickness could occur when two S-layer tubes lie one upon the other. Obviously, the height resolution given by the noise of 0.06 rad is much better than the step height visible at the top of the layer. The phase shift for the double layer step amounts to 0.63 rad with an error of about 10%.

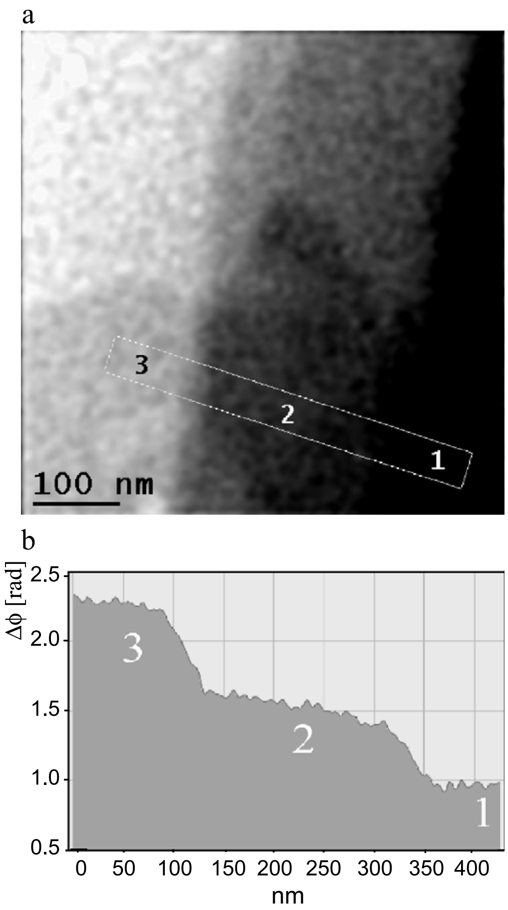

Fig. 6. (a) Reconstructed phase image of electron hologram of the surface layer protein. Since the phase is sensitive to thickness variations, the topography will be registered exceedingly. The bright area represents the S-layer protein self-assembly product, which features a disruption at the right. The double layer constitution of the crystal sheet is demonstrated by the height profile (panel b), which runs normal to the edges of the sheet. Area 1 represents vacuum, 2 is the double and 3 indicates four layers. (b) Height profile of region marked in panel a. Two steps can be clearly recognised representing the double and fourfold layered area. The phase shift for the four layers amount to 1.26 rad with a tolerance of about ~ 0.06 rad (~ 5%) given by the noise visible at the top of the layer. The height resolution of 0.06 rad is in good agreement with the value of about 0.07 rad given in Ref. [15].

4. Conclusions

Off-axis electron holography was proven a suitable tool to image weak phase objects such as unstained surface layer protein crystal lattices. In the reconstructed phase image the lattice planes are clearly visible. As shown by Fourier transform of the phase image, the four first-order spots of the diffraction pattern corresponding to the crystal lattice are present. Furthermore, a single protein sheet of about 5 nm thickness can reliably be determined from the corresponding phase shift. This value corresponds to the one determined by scanning force microscopy [46].

Of course, there exist several alternative methods for thickness determination especially those which make use of the reflection technique such as neutron or X-ray reflectivity and ellipsometry. However, for these methods one needs rather smooth layer systems. At atomic and molecular scale, only scanning force microscopy is able to provide reliable thickness information. Due to careful calibration, the error in height amounts less than 5%. Electron holography suffers like ellipsometry, the same drawback that only the product of thickness and refractive index can be observed. Thus, the mean inner potential of the protein has to be estimated since the lack of experimental values for biological samples.

The lateral resolution reachable with electron holography, in particular when including aberration correction, is superior to conventional microscopy. With inorganic objects, about 0.12 nm have been proven [28]. In our experiments, however, resolution is limited by several factors, which are caused partly by the experimental set-up and mainly by the object characteristics. Instabilities of the microscope, mechanical instabilities, external stray fields or the correct alignment of the biprism with respect to the illumination blur fringe contrast of the hologram and produce additional noise. Thus, stability and elimination of stray fields are required. At the specially designed Triebenberg Laboratory we have a minimum possible disturbance level resulting in a phase detection limit of about $2\pi/60$ at the middle resolution range.

Off-axis holography is not restricted to air dried or freeze dried samples. However, embedding in ice brings several drawbacks as demonstrated in the publications of Harscher [33] or Weierstall and Lichte [31]. Firstly, the contrast between ice and protein is much lower than between air and protein since the object is embedded in a medium with similar refractive index. Secondly, if the vitrified sample is irradiated with a higher dose such as 45 e Å^{-2}, bubbling occurs in the ice layer. Thirdly, for the reference wave, a hole has to be burnt in the ice in the vicinity of the sample. This can be done using a higher dose rate, holding the danger of damaging the sample nearby. At last, since the ice layer consist of lighter elements, inelastic electron scattering predominates. Therefore, the contrast of the interference fringes will be reduced remarkably.

In our case main restriction of resolution is given by the beam sensitivity of the specimen. In order to assess the achievable resolution d, the following equation is used given by Glaeser:

$$d = \frac{1}{C}\frac{5}{\sqrt{fN_{\mathrm{cr}}}} \qquad (2)$$

C, contrast factor ~ 0.1; f, net utilisation factor ~ 0.25; N_{cr}, critical dose.

Because of the beam sensitivity of proteins, only a little dose of about 1–10 e $\mathrm{Å}^{-2}$ can be applied. For example, if a dose of 10 e $\mathrm{Å}^{-2}$ is applied, one should resolve about 3 nm as smallest object detail. In holography, C should be even higher than 0.1 and thus more favourable than in conventional microscopy.

Beam damage is the limiting factor for achievable resolution of proteins both for electron holography and for conventional electron microscopy. Therefore, it is interesting to have a look at the maximum resolution available in conventional TEM. A nice overview about the achieved resolution of 2D and 3D protein crystals by electron microscopy is given by Ellis and Hebert [48]. Cheong et al. [49] achieved on a similar system (surface protein layer of an archeon) a resolution of about 1 nm by applying low temperatures (-120 °C) and spot scan illumination. The total dose amounted to about 1 e $\mathrm{Å}^{-2}$. Kimura et al. [50] imaged the surface of bacteriorhodopsin with a resolution of about 4 Å. They used very low temperatures (4.2 K), the low dose technique and an acceleration voltage of 400 kV. The total dose amounted to about less than 10 e $\mathrm{Å}^{-2}$. Thus, by using a cooling holder, by applying low dose techniques and by embedding the sample into a polymer matrix combined with higher acceleration voltages, one should able to reach at maximum a resolution of 4 Å. This means a factor of 30 better than the 12 nm achieved in our publication at room temperature. In this way, a rather precise identification of the binding sites of the metal particles on the surface layer protein would be possible at almost atomic level.

In theory, by means of holography, it is possible to achieve good contrast from very large spacings down to 3 Å resolution at the same time as given by the phase transfer function cos(χ). In conventional microscopy, very large spacings and finer object details cannot be imaged at the same time due poor contrast at lower spatial frequencies of the PCTF sin(χ). Finally, the correlation of applied dose and achievable resolution for holography has to be assessed and discussed in further investigations and theoretical work [51].

In order to get an insight on the binding area of nanoparticles on the S-layer, which acts as biotemplate, the next step should encompass to image the crystal structure by electron holography at higher resolution up to spacings, which correspond to the higher order and mixed reflections up to 2–3 nm spacing. In this way, the structure of the non-stained S-layer template covered by the regular array of metal particles need not be compared any more with a micrograph of a stained sample in order to locate the binding site of the nanoparticles.

Of course, we could think of not only imaging crystalline samples alone but all kinds of biological systems such as bacteria and virus or cell organelles. By electron holography, a big prospect opens up by imaging unstained biological specimens by their topography or chemical composition.

Acknowledgements

R.W., M.M. and W.P. acknowledge the Deutsche Forschungsgemeinschaft (grant: PO392/18), and the EU (contract: G5RD-CT-2002-0750) for financial support. We would like to thank M. Lehmann for support at the Triebenberg Laboratory.

References

[1] U.B. Sleytr, P. Messner, D. Pum, M. Sara, Crystalline Bacterial Cell Surface Proteins, Academic Press, San Diego, 1996.

[2] H. Engelhardt, J. Peters, Structural research on surface layers: a focus on stability, surface layer homology domains, and surface layer cell wall interactions, J. Struct. Biol. 124 (1998) 276–302.

[3] M. Sara, U.B. Sleytr, S-layer proteins, J. Bacteriol. 182 (2000) 859–868.

[4] A.K. Kotiranta, H. Ito, M.P.P. Haapasalo, K. Lounatmaa, Radiation sensitivity of *Bacillus cereus* with and without a crystalline surface protein layer, FEMS Microbiol. 179 (1999) 275–280.

[5] K. Douglas, N.A. Clark, K.J. Rothschild, Biomolecular solid-state nanohetero-structures, Appl. Phys. Lett. 56 (1990) 692–694.

[6] A.A. Gorbunov, M. Mertig, R. Kirsch, H. Eichler, W. Pompe, H. Engelhardt, Nanopatterning by biological templating and laser direct writing in thin laser deposited films, Appl. Surf. Sci. 109/110 (1997) 621–625.

[7] W. Pompe, M. Mertig, R. Kirsch, A.A. Gorbunov, A. Sewing, H. Engelhardt, A. Mensch, Proc. SPIE 2779 (1996) 72–77.

[8] W. Pompe, M. Mertig, R. Kirsch, H. Engelhardt, T. Kronbach, Functionalized biomolecular membranes for microreactors, in: W. Ehrfeld (Ed.), Microreaction Technology, Springer Verlag, Berlin, 1998, pp. 104–111.

[9] S. Dieluweit, D. Pum, U.B. Sleytr, Formation of a gold superlattice on an S-layer with square lattice symmetry, Supramol. Sci. 5 (1998) 15–19.

[10] W. Shenton, D. Pum, U.B. Sleytr, S. Mann, Synthesis of cadmium sulphide superlattices using self-assembled bacterial S-layers, Nature 389 (1997) 585–587.

[11] M. Mertig, R. Kirsch, W. Pompe, H. Engelhardt, Fabrication of highly oriented nanocluster arrays by biomolecular templating, Eur. Phys. J., D At. Mol. Opt. Phys. 9 (1999) 45–48.

[12] R. Wahl, M. Mertig, J. Raff, S. Selenska-Pobell, W. Pompe, Electron-beam induced formation of highly ordered palladium and platinum nanoparticle arrays on the S-layer of *Bacillus sphaericus* NCTC 9602, Adv. Mater. 13 (2001) 736–740.

[13] M. Mertig, R. Wahl, M. Lehmann, P. Simon, W. Pompe, Formation and manipulation of regular metallic nanoparticle arrays on bacterial surface layers: an advanced TEM study, Eur. Phys. J., D At. Mol. Opt. Phys. 16 (2001) 317–320.

[14] E. Völkl, L.F. Allard, D.C. Joy (Eds.), Introduction to Electron Holography, Kluwer Academic/Plenum Publishers, New York, 1999, pp. 267–293.

[15] H. Lichte, H. Banzhof, R. Huhle, in: H.A. Calderon (Ed.), Proc. ICEM 14, Cancun Mexico I, Institute of Physics, Bristol, Philadelphia, 1998, p. 559.

[16] P. Simon, R. Huhle, M. Lehmann, H. Lichte, D. Mönter, T. Bieber, W. Reschetilowski, R. Adhikari, G.H. Michler, Electron holography on beam sensitive materials: organic polymers and mesoporous silica, Chem. Mater. 14 (2002) 1505–1514.
[17] K. Kato, Osmium tetroxide fixation of rubber lattices, J. Polym. Sci. Polym. Lett. 4 (1966) 35.
[18] J.R. Harris, The negative staining carbon-film procedure—technical considerations and a survey of macromolecular applications, Micron Microsc. Acta 22 (1991) 341–359.
[19] A. Bremer, C. Henn, A. Engel, W. Baumeister, U. Aebi, Has negative staining still a place in biomacromolecular electron microscopy, Ultramicroscopy 46 (1992) 85–111.
[20] P.N.T. Unwin, R. Henderson, Molecular-structure determination by electron-microscopy of unstained crystalline specimens, J. Mol. Biol. 94 (1975) 425.
[21] J. Petermann, H. Gleiter, Direct observation of amorphous and crystalline regions in polymers by defocus imaging, Philos. Mag. 31 (1975) 929–934.
[22] D.L. Handlin, E.L. Thomas, Phase contrast imaging of styrene-isoprene and styrene-butadiene block copolymers, Macromolecules 16 (1983) 1514–1525.
[23] C.L. Woodcock, W. Baumeister, Different representations of a protein-structure obtained with different negative stains, Eur. J. Cell Biol. 51 (1990) 45–52.
[24] W.H. Massover, P. Fun Lai, P. Marsh, Negative staining permits 4.0 angstrom resolution with low-dose electron diffraction of catalase crystals, Ultramicroscopy 90 (2001) 7–12.
[25] H. Lichte, Electron interference: mystery and reality, Philos. Trans. R. Soc. Lond., A 360 (2002) 897–920.
[26] H. Lichte, M. Lehmann, Electron Holography: A Powerful Tool for Analysis of Nanostructures, Advances in Imaging and Electron Physics, vol. 123, Elsevier Science, USA, 2002, pp. 225–255.
[27] P. Simon, H. Lichte, J. Drechsel, P. Formanek, A. Graff, R. Wahl, M. Mertig, R. Adhikari, H.G. Michler, Electron holography of organic and biological materials, Adv. Mater. 15 (2003) 1475–1481.
[28] M. Lehmann, H. Lichte, Tutorial on off-axis electron holography, Microsc. Microanal. 8 (2002) 447–466.
[29] T. Kawasaki, J. Endo, T. Matsuda, N. Osakabe, A. Tonomura, Applications of holographic interference electron-microscopy to the observation of biological specimens, J. Electron Microsc. 35 (1986) 211–214.
[30] K. Aoyama, Q. Ru, Electron holographic observation for biological specimens: electron holography of bio-specimens, J. Microsc. 182 (1996) 177–185.
[31] U. Weierstall, H. Lichte, Electron holography with a superconducting objective lens, Ultramicroscopy 65 (1996) 13–22.
[32] K. Aoyama, G. Lai, Q. Ru, Electron holographic observation of thin biological filaments, J. Electron Microsc. 43 (1994) 39–41.
[33] A. Harscher, Electron holography of biological objects: basics and examples of applications, PhD Thesis, University of Tübingen, Germany, 1999.
[34] U. Weierstall, J.C.H. Spence, M. Stevens, K.H. Downing, Point-projection electron imaging of tobacco mosaic virus at 40 eV electron energy, Micron 30 (1999) 335–338.
[35] H.W. Fink, H. Schmid, E. Ermanntraut, T. Schulz, Electron holography of individual DNA, J. Opt. Soc. Am. A 14 (1997) 2168–2172.
[36] T. Matsumoto, T. Tanji, A. Tonomura, Visualisation of DNA in solution by Frauen-hofer in-line electron holography: 2. Experiments, Optik 100 (1995) 71–74.
[37] E. Knapek, Properties of organic specimens and their supports at 4 K under irradiation in an electron microscope, Ultramicroscopy 10 (1982) 71–86.
[38] Workshop on High-Resolution Electron Microscopy, Betheseda, MD, USA, 2000, http://em-outreach.sdsc.edu/web-course.
[39] D.T. Grubb, Radiation damage of organic materials in the transmission electron microscope, Ultramicroscopy 12 (1984) 279–280.
[40] E. Kellenberger, The ups and downs of beam damage, contrast and noise in biological electron microscopy, Micron Microsc. Acta 17 (1986) 107–114.
[41] J. Brink, H. Gross, P. Tittmann, M.B. Sherman, W. Chiu, Reduction of charging in protein electron cryomicroscopy, J. Microsc. 191 (1998) 67–73.
[42] H. Stark, F. Zemlin, C. Boettcher, Electron radiation damage to protein crystals of bacteriorhodopsin at different temperatures, Ultramicroscopy 63 (2) (1996) 75–81.
[43] T. Ohno, Intensity changes induced by beam damage in electron diffraction from behenic acid multiple monolayers, Ultramicroscopy 48 (1993) 359–363.
[44] E. Knapek, H. Formanek, G. Lefranc, I. Dietrich, The interpretation of radiation damage measurements with electron diffraction of organic materials at very low temperatures, Ultramicroscopy 14 (1984) 253–264.
[45] R.M. Glaeser, K.A. Taylor, Radiation damage relative to transmission electron microscopy of biological specimens at low temperature: a review, J. Microsc. 112 (1977) 127–138.
[46] M. Mertig, R. Wahl, unpublished results.
[47] Y.C. Wang, T.M. Chou, M. Libera, E. Voelkl, B.G. Frost, Measurement of polystyrene inner potential by transmission electron holography, Microsc. Microanal. 4 (1998) 146–157.
[48] M.J. Ellis, H. Hebert, Structure analysis of soluble proteins using electron crystallography, Micron 32 (2001) 541–550.
[49] G.W. Cheong, D. Typke, W. Baumeister, Projection structure of the surface layer of *Methanoplanus limicola* at 10 angstrom resolution obtained by electron cryomicroscopy, J. Struct. Biol. 117 (1996) 138–144.
[50] Y. Kimura, D.G. Vassylyev, A. Miyazawa, A. Kidera, M. Matsushima, K. Mitsuoka, K. Murata, T. Hirai, Y. Fujiyoshi, Surface of bacteriorhodopsin revealed by high-resolution electron crystallography, Nature 389 (1997) 206–211.
[51] H. Lichte, What atoms are where? Which fields are around? Proc. Micro. Microanal. 9 (Supplement 2) (2003) 768CD–769CD, Cambridge Univ. Press, Cambridge, UK.